Strengthening and Toughening Epoxy Polymer at Cryogenic Temperature using Cupric Oxide Nanorods

Wenkai Chang[a], L. R. Francis Rose[b], Mohammad S. Islam[a], Shuying Wu[a, c], Shuhua Peng[a], Feng Huang[a], Anthony J. Kinloch[d], Chun H. Wang[a*]

[a] School of Mechanical and Manufacturing Engineering, University of New South Wales, Sydney, NSW 2052, Australia.

[b] Defence Science and Technology Group, Melbourne, VIC 3207, Australia.

[c] School of Engineering, Macquarie University, Sydney, NSW 2109, Australia.

[d] Department of Mechanical Engineering, Imperial College London, South Kensington Campus, London SW7 2AZ, U.K.

Abstract

At cryogenic temperatures thermoset polymers suffer from low fracture toughness. Herein, we present a strengthening and toughening technique for cryogenic applications using cupric oxide (CuO) nanorods. These nanorods are synthesized via a hydrothermal reaction to give an average length of 1.64 μm and a diameter of 270 nm. They exhibit a low coefficient of thermal expansion (CTE) at cryogenic temperatures, due to the magnetostriction effect. Epoxy nanocomposites containing up to 8 wt% of CuO were investigated. Both the tensile strength and the fracture energy were found to increase with CuO content up to 4 wt%, showing improvements of 18% and 132% respectively at room temperature, and of 21% and 262% at -196°C. Current theoretical models were shown to account for the experimentally measured values of both strength and toughness at room temperature, but to significantly underestimate the observed values at -196°C. However, modifications of these models to include thermal residual stresses generated by the CTE mismatch are proposed that lead to good agreement with the measured values. The technique to strengthen and toughen epoxy using CuO nanorods and the modified theories provide potential for designing and optimising multi-scale fibre composites for cryogenic applications such as cryogenic fuel tanks.

Keywords: Nano composites; Cryogenic engineering; Fracture toughness; Material modelling

*Corresponding author: Chun-Hui Wang (E-mail: chun.h.wang@unsw.edu.au Tel: +61 2 93853232)

1. Introduction

Lightweight fibre-reinforced polymer (FRP) composites, typically with an epoxy matrix, are receiving strong interest in cryogenic engineering applications such as cryogenic propellant vessels for space shuttles and superconducting solenoid technologies. However, despite offering many desirable properties, thermoset epoxy polymers have a relatively low fracture toughness and hence poor resistance to cracking at cryogenic temperatures [1]. The low strength and fracture properties of epoxy-based FRPs hinder their applications for storing cryogenic liquids such as liquid hydrogen (at -253°C), liquid nitrogen (at -196°C) and liquid oxygen (at -183°C) [2]. To enable cryogenic applications of epoxy fibre-composites, it is important to enhance their damage tolerance, i.e. fracture toughness [3], and to suppress matrix microcracking under super cold temperatures [4, 5]. One major method to improve the mechanical and fracture properties of epoxies at cryogenic temperatures, i.e. below -150°C [6], is to incorporate a nano/micro-scale hard phase which can enhance the strength as well as the toughness [3]. In this regard, most research to date has focused on the strengthening epoxies at cryogenic temperatures [1, 7-13], with only a few reports on toughening [5, 11-13]. For example, nanoclays [7], nano-SiO_2 particles [8, 12] and carbon nanomaterials, including carbon nanotubes (CNTs) [1, 13], graphene nanoplatelets (GNPs) [9] and graphene oxide (GO) [5, 10] have been demonstrated to strengthen epoxy polymers at temperatures below -183°C. Some of these studies [1, 8-10, 13] have identified the fact that the localized compressive thermal residual stress between the epoxy matrix and fillers caused by the mismatch between their coefficients of thermal expansion (CTE) has a positive effect on the strength of the epoxy. Furthermore, in addition to a strengthening and stiffening effect, a hard nano/microphase also provides localized toughening, without reducing the glass transition temperature of the epoxy [3, 14, 15]. For instance, CNTs [13], nano-SiO_2 [12], GO platelets [5] and nano-ZrO_2 [11] have demonstrated potential in toughening epoxy polymers at temperatures below -183°C. However, these reported levels of improvement in the fracture energies of epoxy polymers are considered to be less than the target level of 100% necessary to suppress matrix microcracking of FRPs at cryogenic temperatures (i.e. below -150°C), since the thermal residual stresses in FRPs at cryogenic temperatures are twice as high as that experienced by aircraft at their minimum operating temperature of -54°C [16].

One effective method to mitigate microcracking of FRP composites is to lower the effective CTE of the epoxy matrix, thereby reducing the CTE mismatch between the epoxy matrix and the reinforcing fibres [5, 17]. In this regard, nanosized cupric oxide (CuO), which is an antiferromagnetic compound, has been reported to exhibit an extremely low, or even negative, CTE at cryogenic temperatures, due to the

magnetostriction effect [18, 19]. This intriguing property may provide additional benefits in both lowering the effective CTE of epoxy composites and, thus, enhancing their strength and fracture toughness [20]. To produce CuO nanoparticles, the hydrothermal synthesis has been demonstrated as a simple and effective method that offers good control over particle shape, size, and reproducibility [21]. In a typical hydrothermal reaction process, the strong polarity of the aqueous reaction solution promotes the oriented growth of nanocrystals, leading to nanomaterials with low-dimensional morphology [21]. Particularly, one-dimensional (1D) CuO nanoparticles (i.e. CuO nanowires or nanorods) have been reported to possess relatively high strengths [22] and elastic moduli [23]. However, to the best of our knowledge, there is no study on the use of CuO nanorods to strengthen and toughen epoxy polymers, neither at room temperature (RT) nor at cryogenic temperatures.

Although recent research [1, 8-10, 13] has recognised the beneficial effect of compressive thermal residual stress at cryogenic temperatures, there is a lack of quantitative models that can adequately account for the thermal residual stresses in the design and optimisation of nanocomposites for use at cryogenic temperatures, either in their own right or as the matrix material for FRPs. For example, previous studies [5, 11-13] on toughening and strengthening epoxy polymers at temperatures below -183°C are mainly experimental. Although, Carolan et al. [15] have reported an analysis of the fracture energy enhancement by nano-SiO_2 particles at -80°C which is based on predictive models [14, 24, 25] developed for ambient-temperature estimations. However, their analysis does not take into account any effects of residual thermal stresses.

Herein, we present a comprehensive study of the effectiveness of CuO nanorods, synthesized using the hydrothermal method, in strengthening and toughening an epoxy polymer at the liquid nitrogen temperature (-196°C) as well as at RT (25°C). Key aspects of material synthesis, characterization and mechanical testing are presented in Section 2. The results of the tensile and fracture energy tests performed at the two different temperatures are presented next in Section 3, including detailed fractographic studies to identify the strengthening and toughening mechanisms responsible for the property improvements observed at both temperatures. In Section 4, existing models for predicting the strength and toughness of particle reinforced epoxy polymers are discussed and are found to significantly underestimate the present experimental results at -196°C, although the correlation is good for the RT results. Therefore, we have developed modifications to the existing models to account for the contributions of the compressive thermal residual stress, which then lead to a good correlation between the modelling and the experimental results.

2. Materials and experimental details

2.1 Synthesis of CuO nanorods

A solution-based hydrothermal synthesis method [21, 26] was employed to fabricate the CuO nanorods, as illustrated in Figs. 1a and b. First, the 7.5 M sodium hydroxide (NaOH, Chem-Supply Pty Ltd, Australia) aqueous solution was dropwise add to the 0.5 M copper nitrate ($Cu(NO_3)_2 \cdot 2.5H_2O$, Chem-Supply Pty Ltd, Australia) ethanol solution in a volume ratio of 1:10 of $Cu(NO_3)_2$ to NaOH solution under continuous stirring, which caused the blue $Cu(NO_3)_2$ solution to become turbid. Secondly, the mixed solution was transferred to a fully sealed Teflon-lined stainless-steel autoclave, which was then heated to 150 °C for 24 h. Finally, the CuO nanorods were collected from the reactor, centrifuged with DI water followed by ethanol, and then dried at 80°C for 12 h.

2.2 Preparation of epoxy nanocomposites

The hydrothermally synthesized CuO nanorods were added to an epoxy resin at various weight fractions, i.e. 1, 2, 4, 8 wt%, relative to the total weight of the epoxy resin and curing agent. The epoxy resin used was Raku Tool EL-2203 (from GMS Composites, Australia) which is a mixture of two bisphenol A-epichlorohydrin epoxies and a bisphenol F-epichlorohydrin resin epoxy, diluted with 1,2,3- propanetriol glycidyl ether. After hand mixing for 5 min, the mixtures were passed through a three-roll mill for three times (with a roller gap: 15 μm and speed: 100 rev/min). Subsequently, the milled CuO/epoxy resin mixtures were further processed by a probe-ultrasonic mixer (Sonics VCX-750 Vibra Cell Ultra Sonic Processor) for 1 h. Then, a curing agent, which was a mixture of three amines, i.e. isophorone diamine, m-xylylenediamine and 2,2,4-trimethylhexane-1,6-diamine (Raku Tool EH-2970-1, GMS Composites, Australia), was added at the manufacturer's recommended stoichiometric quantity to the epoxy resin [27], i.e. the mix ratio in parts by weight was 30:100 of curing agent:epoxy resin. The liquid mixtures were then mixed manually for 5 min followed by 10 min degasification. Lastly, the mixtures were cast in moulds to produce the test specimens. All the specimens were cured at RT for 24 h.

2.3 Characterization of hydrothermally synthesized CuO nanorods

The morphology and elemental analysis of the hydrothermally synthesized CuO nanorods were characterized using a scanning electron microscope (FEI Nova SEM 230) equipped with an energy dispersive X-ray (EDX) detector. The phase structure of the fabricated CuO nanorods was characterized using X-ray powder diffraction (XRD) analysis (PANalytical Empyrean-2 XRD System with Cu Kα radiation, λ=1.54 Å). To determine the effect of temperature on the lattice parameters of the nanocrystals, isothermal XRD measurements were conducted using a PANalytical Empyrean-1 XRD instrument

equipped with a cryostat (Oxford PheniX). The XRD data were collected at temperatures below (20, 77 and 140 K) and above (220, 260 and 298 K) the CuO magnetic ordering temperature (or Néel temperature, T_N) of 212 K [28] over the 2θ range of 20° to 80°, using a step angle of 0.02°. The lattice parameters at different temperatures were determined by undertaking the Rietveld refinement of each XRD spectrum with PANalytical HighScore Plus software, whereby the values of the linear CTE were determined by the change in the lattice constants with temperature (see Supplementary Information).

2.4 Tensile and fracture energy testing

Dumbbell tensile specimens were manufactured according to the 'Type IV specimen configuration' of ASTM D638 [29] shown in Fig. 2a. Uniaxial tensile tests were conducted using a universal testing machine (Instron 3369) with a displacement rate of 1 mm/min in accordance with ASTM D638 [29]. The cryogenic temperature (-196°C) tensile testing was achieved by immersing the specimens, fixed in the grips, in a liquid nitrogen-filled cryostat. Before testing the dumbbell tensile specimens in the liquid nitrogen bath they were allowed to equilibrate in the liquid nitrogen for 15 minutes. At least three replicate tensile specimens were tested for each formulation.

The mode I fracture energy, G_{Ic}, of the materials was measured using double cantilever beam (DCB) adhesively-bonded joint tests in accordance with ISO 25217 [30]. As illustrated in Fig 2b, a relatively thick (i.e. 2.5 mm) epoxy nanocomposite layer is sandwiched between two laminated composite adherends. This DCB-bonded joint configuration encourages the crack to remain within the epoxy layer. The adherends (also 2.5 mm in thickness) were manufactured using 12 plies of unidirectional T700 carbon-epoxy prepreg (VTM264, Lavender Composites, Australia). The surfaces of the cured laminates were abraded using aluminium-oxide abrasive paper and then cleaned with isopropyl alcohol. At one end of the DCB-bonded joint, a polytetrafluoroethylene (PTFE) film (11 μm thick) was placed at the mid-plane of the nanocomposite layer. The tests consisted of an initial loading and re-loading using an Instron universal test machine (Instron 3369) with a 1 kN capacity loadcell. The specimens were initially loaded at a displacement rate of 1 mm/min to generate a naturally sharp pre-crack by extending the initial crack length from the PTFE insert to 10 ± 2 mm, followed by complete unloading. The pre-cracked specimens were subsequently re-loaded by applying a continuously increasing displacement at a rate of 1 mm/min. The DCB-bonded joints pinned on the loading points were immersed into liquid nitrogen to measure G_{Ic} at -196°C. The DCB specimens were allowed to equilibrate in the liquid nitrogen for 15 minutes prior testing at -196°C. The crack was observed to propagate cohesively within the nanocomposite layer. The values of G_{Ic} were calculated using the "corrected beam theory" method described in ISO 25217 [30]. Here $G_{Ic} =$

$3P\delta F/(2BN(a+|\Delta|))$, and P denotes the load, δ the cross-head displacement, a the total crack length from the loading line, and b the sample width; Δ, F and N are the correction factors defined in [30], which take into account the specimen compliance and the influence of using load blocks. The crack propagation length, a, was monitored using a digital microscope camera. At least three replicate specimens were tested for each type of material.

3. Experimental results and discussion

3.1 Characterization of hydrothermally synthesized CuO nanorods

The typical morphology of synthesized CuO is shown in the scanning electron micrograph (SEM) in Fig. 1c. It is worth noting that the synthesized material exhibited an elongated rod-like structure with square or nearly circular cross-sections. The majority of the CuO particles had a length of 0.5 to 3 μm and a diameter of 50 to 500 nm with the average aspect ratio (i.e. length/diameter) of six in the present work. (In accordance with the 'IUPAC Recommendations' [31] these dimensions justify their designation as 'nanorods' and, indeed, this terminology is used throughout the published literature on these materials [e.g. 21-23, 26, 28].) A similar structure was reported for CuO by Shrestha et al. [26] using similar synthesis conditions. The elemental composition of the nanorods was characterized using EDX. As shown in Fig. 1d, the EDX spectrum confirms the presence of Cu and O elements which are in an atomic ratio of approximately 1:1. The detected silicon and carbon elements can be attributed to the silicon-wafer substrate and carbon coating used to assist the SEM-EDX characterization. Figs. 3a, b present the probability density distributions of the length and diameter of the CuO nanorods, respectively. The two-parameter (i.e. the scale parameter, c, and shape parameter, k) Weibull distribution function was used for modelling the nanorod length in μm (with $f(l)$, $c = 1.83$ and $k = 2.87$) and the diameter in nm (with $f(d)$, $c = 304.27$ and $k = 3.23$). The phase structure of the prepared nanorods was characterized using XRD. The XRD pattern shown in Fig. 3c is fully consistent with the card ICDD#04-015-5868, confirming the formation of CuO with a monoclinic crystal structure (see Fig. 3d). The sharp diffraction peaks indicate the highly pure and highly crystalline CuO, with no impurity peaks evident in the CuO nanorods.

The temperature dependences of five lattice parameters for the CuO nanorods normalized by their respective values at 25°C are shown in Fig 3e. It is important to note that there are abrupt steps observed around T_N on the temperature dependence curves. This was also confirmed by [18, 19] in which the magnetolattice coupling was found to be the cause for the apparent anomalies in the lattice constants. The results showed that none of the unit cell parameters changed significantly when the nanocrystals were

cooled to below T_N, indicating that the thermal expansion of CuO nanorods approached zero with decreasing temperature. Table 1 shows the axial and transverse CTE values of the CuO nanorods, which indicates the anisotropic thermal expansion of nanorods due to the monoclinic crystal structure of CuO. At temperatures above T_N, consistently positive CTEs were observed in three dimensions. On cooling below T_N, however, the CuO nanorods exhibited an extremely low CTE along the axial direction and almost zero, or even negative, CTEs in the transverse directions. A similar vanishing thermal expansion at low temperatures has also been reported for various magnetic crystal materials in [20]. From the study by Zheng et al. [18], the vanishing and even negative thermal expansion effect below T_N may arise from the magnetostriction effect in CuO nanocrystals. This means that as the temperature decreases below T_N, lattice expansion emanating from magnetic reordering can occur and this expansion may exceed the contraction caused by the temperature drop. This magneto-lattice coupling has been considered a major mechanism for the negative CTE phenomenon [20]. The extremely low CTEs of CuO nanorods at cryogenic temperature also result in low average CTEs in the temperature range of -196 to 25°C (77 to 298 K), as listed in Table 1, which are more than ten times lower than the typical CTE of epoxy (i.e. 65×10^{-6} K^{-1} [5]).

3.2 Tensile properties

The stress versus strain curves of the neat epoxy and epoxy nanocomposites containing different weight contents of CuO nanorods at RT and -196°C are shown in Fig. 4. The CuO-modified epoxy nanocomposites exhibited both a higher strength and higher failure strain than the neat epoxy. The epoxy polymers exhibit a slight non-linear failure behaviour at RT (see Fig. 4a) whilst at -196°C, in contrast, they show completely linear stress versus strain curves with abrupt load drops, as shown in Fig. 4b. These observations reveal the very brittle behaviour of the epoxy polymers. Furthermore, the neat epoxy and epoxy nanocomposites all failed at very low strain levels (less than 2 %) at -196°C, showing apparent cryogenic embrittlement which is ascribed to the restrained mobility of the polymer chains due to less free volume in the frozen epoxy network at cryogenic temperatures [1, 12, 32], see Fig. S7.

The experimental results, including the Young's modulus and ultimate tensile strength, obtained at RT and -196°C are shown in Fig. 4c in terms of the CuO weight content. For the nanocomposites both the elastic modulus and tensile strength first increased with the CuO content, reaching their respective maximum value at 4 wt%, followed by a decline, with the results at 8 wt% being smaller or similar to those at 4 wt% content. This is attributed to the inadequate dispersion of nanorods at high loading level due to the increase in viscosity (see Figs. S3, S6) and the resulting agglomeration of nanorods would be likely to cause high stress concentrations and reductions in mechanical properties [33]. As shown in Fig. 4c, the

Young's modulus results at 8 wt% are similar to those at 4 wt% content and this difference is not statistically significant. Thus, up to a 9% and 8% increase in stiffness were obtained at RT and -196°C, respectively, with a nanorod content of 4 wt%. Moreover, the Young's modulus of the epoxy at -196°C was substantially greater than that at RT, which is consistent with the results reported in the literature for other epoxy polymers [1, 9, 12, 13]. The significantly higher stiffness observed at cryogenic temperature is mainly attributed to the polymer chains becoming more rigid and compact at cryogenic temperatures [13].

The effects of the nanoscale reinforcement on the Young's modulus, E_{com}, of the resultant nanocomposites can be explained and quantified using theoretical models for short fibre reinforcement. Some recent efforts [34, 35] have extended the modulus and strength models of short fibre polymer composites to take into account the contributions by micro/nano-scale 1D fillers. Thus, the elastic modulus was estimated using the modified Rule of Mixtures [36] and the Halpin-Tsai models [37], and the details are given in the Supplementary Information. A comparison of the predicted and experimental values is presented in Fig. 4c, which shows that the predictions by both models are in very good agreement with the measured values.

At both RT and -196°C, the tensile strength of the epoxy nanocomposite increased with the nanorod weight content up to 4 wt% (see Fig. 4d). The epoxy nanocomposites were consistently stronger at -196°C than at RT. This is mainly because the crosslinked network of epoxy matrix shrinks and the intermolecular binding forces significantly increase at the cryogenic temperatures [13], leading to the higher strength at -196°C (i.e. 70.10±5.33 MPa) than that at RT (i.e. 54.72±4.54 MPa) for the epoxy polymer. Moreover, it was found that the maximum percentage improvements in strength relative to the neat epoxy at -196°C (i.e. 21%) is higher than that at RT (i.e. 18%), indicating a higher reinforcing performance of the CuO nanorods at cryogenic temperatures. This can be attributed to higher interfacial failure stresses being present at -196°C, due to the compressive thermal residual stresses caused by the CTE mismatch between the epoxy matrix and the CuO nanorods. This is supported by the SEM images of the tensile fracture surfaces, showing that the nanorods are cleanly pulled-out from the epoxy at RT, with smooth surfaces being observed (see Figs. 5a, b), whereas relatively rough surfaces covered with retained epoxy fragments were observed at -196°C (see Figs. 5c, d). No nanorod was found to rupture, indicating that the nanorods are shorter than the critical length, l_c, for fracture according to the Kelly-Tyson formula [38] of $l_c = \sigma_r d_r / 2\tau_i$, where σ_r and τ_i are the nanorod strength and the interfacial shear strength, respectively, and d_r is the nanorod diameter. Polyakov et al. [22] have reported that the intrinsic strength of 1D nano-CuO to be 6.5 GPa. The interfacial shear stress, τ_i, cannot exceed the shear strength of the epoxy, which can be approximated by half of the

tensile strength of the neat epoxy [39]. This leads to conservative estimates for the critical length l_c = 32 μm at RT and 25 μm at -196°C, which are considerably larger than the average length of the nanorods of 1.64 μm.

3.3 Fracture energy

Typical load versus crack opening displacement (P-δ) curves measured during the re-loading stage of DCB-joint tests of the neat epoxy and nanocomposites at RT and -196°C are shown in Figs 6a, b, respectively. The "saw-tooth" shaped P-δ curves are indicative of stick-slip crack growth behaviour. The values of the mode I critical fracture energy, G_{Ic}, of the neat epoxy and epoxy nanocomposites at RT and -196°C are shown in Fig 6c. The fracture energy increased almost linearly with the weight content of nanorods up to 4 wt%, reaching the highest improvements at RT of 132%, and at -196°C of 261%. As the weight content of CuO increased to 8 wt%, the G_{Ic} value decreased, which may be caused by the agglomeration of nanorods at the higher concentration levels. As shown in Fig. 6c, the G_{Ic} values of all the specimens measured at -196°C were consistently lower than those for the same filler content at RT, confirming the intuitive expectation that the epoxy polymers are more brittle at cryogenic temperatures. However, the relative improvement in G_{Ic} was more pronounced at -196°C than at RT. A similar observation was also reported in [15] for the addition of nano-SiO_2 particles, and it can be attributed to the influence of thermal residual stresses, as further discussed in Section 4.

Furthermore, at a given weight content of CuO, the increase in G_{Ic} of the epoxy nanocomposite relative to that of neat epoxy at -196°C appeared to be similar to the increase at RT. To further illustrate this, the measured fracture energies at the two test temperatures are plotted together in Fig. 6d. The rates of increase in the values of G_{Ic} at RT and -196°C with the increased content of nanorod are approximately the same, with the experimental data lying close to the line indicating a 1:1 relationship; the offset can be attributed to the lower toughness of the epoxy matrix at -196°C than RT.

With respect to the mechanical performance of this epoxy nanocomposite at RT and a cryogenic temperature, a comparison with other epoxies reinforced by other reported hard nano/micro-fillers [5, 11-13, 40-42] is shown in Fig. 7 in which the highest percentage improvements (relative to the neat epoxy) in fracture toughness and tensile strength are given. Clearly, the epoxy nanocomposites investigated in the present study demonstrate a favourable combination of fracture toughness and strength, especially at cryogenic temperatures.

3.4 Toughening mechanisms

Post-failure examination was performed of the crack initiation regions in the DCB-joint specimens tested at RT and -196°C to identify the toughening mechanisms induced by the addition of the CuO nanorods. Firstly, the SEM images shown in Fig. 8 clearly indicate that the fracture surfaces of the nanorod-modified epoxy are much rougher than those of the neat epoxy at both temperatures. More detailed examination of the fracture surfaces for the nanocomposites at high magnifications, as shown in Fig. 9, reveal that the main toughening mechanisms induced by the presence of the CuO nanorods, irrespective of the testing temperature, include (a) interfacial debonding of the nanorods from the epoxy, (b) pull-out of the nanorods, (c) plastic void growth and (d) localized shear yielding of the epoxy. As indicated in Figs. 9a, b and d, e, nanorods are debonded and pulled-out from the epoxy matrix normal and oblique to the fracture plane, leaving behind voids on the fracture surface. This also incurs some energy dissipation [43].

A large number of voids were observed in the SEM images (see Fig 9) with their diameters being greater than that of the nanorods, indicating that plastic void growth had taken place during, or following, the pull-out. The plastic deformation of the epoxy accompanying void-growth also dissipates energy, which can be more than that due to debonding, according to previous estimates [14, 44]. Moreover, at the highest nanorod content investigated in the present study (i.e. 8 wt%), the void growth was observed to be affected by the agglomeration (see Fig. 9c), which results in the reduction in the toughening effect observed in Fig. 6c.

At both test temperatures, plastic deformation of the matrix may occur following debonding of the CuO nanorods, which leads to the voids that are observed on the fracture surfaces. This arises since, in the dissipation zone ahead of the crack tip, the nanorods tend to debond and the surrounding epoxy polymer is now less constrained and more readily undergoes plastic deformation. In addition, as indicated by the solid yellow arrows in Fig. 9, the tail structures behind the voids and nanorods are formed by the convergence of two secondary crack fronts which are separated by a void or nanorod. In general, there is a high degree of similarity between the fracture surfaces from tests undertaken at RT and -196°C. However, one difference observed between these two test temperatures is that a clean pull-out, with no epoxy retained on the surfaces of the nanorods, and full debonding of the nanorods is seen from the RT tests (see Figs. 9a-c). However, at -196°C, the SEM micrographs of the fracture surfaces reveal that large areas of the surfaces of the nanorods are covered with retained epoxy fragments (see Fig. 9e), and some nanorods distributed in the fracture plane are only partially debonded, or are still bonded within the epoxy, which then causes the fracture of the epoxy, as noted by the sharp fracture surface features shown in Fig. 9f.

4. Modelling

4.1 Strength

The Fu et al. strength model [45] for randomly oriented short fibre composites, based on a rule of mixtures approach, was used to predict analytically the tensile strength, σ_{com}, of the epoxy nanocomposites containing CuO nanorods. Since the nanorods in the present study are much shorter than the critical length, as noted in Section 3.2, this estimate for σ_{com} can be expressed in terms of the interfacial frictional stress, τ_i, and the ultimate tensile strength of the neat epoxy, σ_m, instead of the fracture strength of the nanorod. Thus:

$$\sigma_{com} = \lambda V_r \tau_i + \sigma_m (1 - V_r) \quad (1)$$

where V_r denotes the volume fraction of nanorods and λ is a load transfer efficiency factor which can be obtained by simplifying the solution represented in [45, 46] to be:

$$\lambda = \frac{4}{\pi d} \int_0^{\frac{\pi}{2}} \int_{l_{min}}^{l_{max}} f(l) \frac{l^2}{2 l_{mean}} e^{\mu\theta} \mathrm{d}l\mathrm{d}\theta \quad (2)$$

where l denotes the nanorod length and μ a snubbing friction coefficient between a nanorod inclined at angle θ to the crack plane and the matrix, which is assigned to be 1.25 in this study, following [44]. The mean nanorod length, l_{mean}, can be readily obtained from the Weibull length distribution function (see Section 3.1). This analytical model assumes that the nanorods are initially elastically bonded to the matrix and would debond, followed by pull-out against the interfacial frictional shear stress, τ_i, during failure of the nanocomposites. As shown by the dashed curves in Fig. 10a, at RT the model predictions from Eq. (1) are in good agreement with the experimental results, with the efficiency factor λ = 21.4 as calculated from Eq. (2). However, at -196°C this model significantly underpredicts the strengthening effect induced by the nanorods. A plausible reason for this underprediction is that the compressive thermal residual stresses induced by the CTE mismatch were neglected in modelling the frictional resistance of the nanorod/epoxy interface. To account for this effect, the bridging stress transmitted by the nanorod at -196°C is modified by including the thermal residual compressive radial stress, σ_r^T, in calculating the load carried by a nanorod crossing the failure plane, so that Eq. (1) now becomes (see Supplementary Information for details):

$$\sigma_{com} = \lambda V_r (\tau_i + \mu_f \sigma_r^T) + \sigma_m (1 - V_r) \quad (3)$$

where μ_f denotes the coefficient of friction, which is taken to be 0.9, using the value given by Jia et al. [47] for carbon fibres in epoxy. A value of 60 MPa for σ_r^T is obtained from a finite element model (FEM) of a representative volume element for the composite subjected to a temperature change ΔT = -221 K (25°C ~ -196°C); further details are provided in the Supplementary Information. The predicted strength from Eq.

(3) with this modification is presented as the solid curve in Fig. 10a. These predictions now show a very much improved agreement with the measured values up to 4 wt% of CuO nanorods, thereby providing evidence that the thermal residual stresses do indeed affect the measured strength at cryogenic temperatures.

4.2 Fracture energy

The fractographic evidence presented in Section. 3.4 indicates that the improvements in the fracture energies at both RT and -196°C can be attributed to the following toughening mechanisms, as shown schematically in Fig. 11: the energy arising from (a) interfacial debonding of the nanorods, ΔG_{db}, (b) pull-out of the nanorods, ΔG_{po}, (c) plastic void growth, ΔG_v and (d) plastic shear yielding, ΔG_s. By combining the fracture energy contributions via these toughening mechanisms with the fracture energy of the neat epoxy, G_{CU}, the fracture energy, G_{Ic}, of the epoxy nanocomposites can be given by [14, 25, 43, 48, 49], $G_{Ic} = G_{CU} + \Delta G_{db} + \Delta G_{po} + \Delta G_v + \Delta G_s$. The analytical estimates for these toughness increments have been proposed in the literature, notably by Kinloch and co-workers [14, 49], who noted that the contributions from plastic void growth and shear yielding are generally the dominant contributions for an epoxy polymer containing rigid fillers. Appropriate estimates for the terms in G_{Ic} for the present work are summarised below and the key parameters used for modelling are listed in Table 2.

Firstly, based on the analysis of Clyne and Hull [50] and Cottrell and Kelly [51], the contribution to the overall fracture energy from the nanorod pull-out mechanism is $\Delta G_{po} = 2V_{po}\tau_i l_{po}^2/d_r$, where V_{po}, given in Table 3, denotes the volume fraction of nanorods that are pulled-out, which has been determined from the SEM micrographs of the fracture surface and following the approach used in [43, 44]. Secondly, the pull-out length of nanorods, l_{po}, is estimated as half the average length, l_{mean}, based on the subcritical fibre length analysis in [50]. The interfacial shear stress, τ_i, is estimated as in Section 3.2 and d_r is taken to be the average nanorod diameter, as listed in Table 2.

Next, the toughness increments due to particle debonding and subsequent plastic void growth were estimated by adapting a model proposed by Williams et al. [52] for the particle toughening of polymers. This model considers cylindrical particles and fibres that are much stiffer than the polymer matrix and which are modelled as being rigid, so that the estimates of the resulting toughness only involve the matrix elastic modulus, E_m and Poisson's ratio, v (taken to be 0.35 [14]). This is a reasonable simplifying assumption for the present work since the Young's modulus for CuO nanorods is reported to be 80 GPa [23], which greatly exceeds the measured values for the epoxy given in Section 3.2. In this model [52], debonding is assumed to initiate and to progress unstably to completion, when the radial stress at the

particle-epoxy interface reaches the critical value, σ_c. By assuming that all particles within the dissipation zone debond, the dissipated strain-energy density associated with debonding, ΔU_{db} is calculated to be [52]:

$$\Delta U_{db} = (1+v)\frac{\sigma_c^2}{E_m}V_r \quad (4)$$

so that the fracture energy increment due to debonding is:

$$\Delta G_{db} = 2h\Delta U_{db} \quad (5)$$

where $h = E_m G_{CU}/2\pi\sigma_c^2$, denotes the height of the dissipation zone for debonding [52, 53]. Lauke [54] has pointed out that experimental observations for a particle reinforced epoxy are consistent with σ_c being a characteristic of the interface, independent of particle size. Accordingly, it is assumed for simplicity, that $\sigma_c = \sigma_m$.

Similarly, the toughening contribution due to plastic void growth is calculated to be:

$$\Delta G_v = 2h\Delta U_v \quad (6)$$

where ΔU_v denotes the dissipated strain-energy density associated with plastic void growth. Based on the analysis of Williams et al. [52, 53], ΔU_v can be expressed as:

$$\Delta U_v = (1+v)\left[\left(V_{void} - V_{po}\right)\sigma_c - \frac{1}{(1-v)}\frac{\sigma_c^2}{E_m}V_{po}\right] \quad (7)$$

where V_{void} denotes the volume fraction of the voids. The fractographic examinations in the present study indicated that voids were left behind by debonded and pulled-out nanorods both normal and oblique to the fracture plane (see Fig. 9). Accordingly, the value of V_{void} was determined by assuming the shape of each void to be a truncated cone, adopting the approach used previously for other 1D nanofillers in [43, 44, 48]. As estimated from the SEM micrographs, the mean diameters of the voids formed at RT and -196°C were approximately 6.9 and 6.3 times larger than the mean nanorod diameter, respectively, which is also comparable with the relative void diameter reported for a carbon nanofibre (CNF)-modified epoxy polymer in [43]; this leads to $V_{void} = \sim 19V_{po}$ and $\sim 16V_{po}$ at RT and -196°C, respectively. The proportion of the nanorods observed to be pulled-out and leave behind voids is similar at two temperatures, as given in Table 3.

Lastly, the fracture energy contribution from the shear yielding of the epoxy matrix was determined from the Huang-Kinloch model [14, 25], where $\Delta G_s = 0.5V_r\sigma_y\gamma F'(r_y)(\sqrt{3}+\mu_m)/(\sqrt{3}-\mu_m)$, and γ denotes the failure strain of the neat epoxy, μ_m is a material constant accounting for the pressure dependency of the epoxy yield stress and σ_y is the tensile yield stress of the epoxy which was assumed to be equal to the ultimate tensile strength, σ_m, (see Table 2), following the approach used in [55]. The term

$F'(r_y)$ is a geometric term given in [14], with the value for the von Mises stress concentration factor of approximately 2.11 [43, 48] for the nanorod volume fractions investigated in the present work.

4.3 Comparison of measured and predicted values of G_{Ic}

Combining the above estimates for the toughening increments leads to the fracture energy predictions in Table 3, which are also shown by the dashed lines in Fig. 10b. It can be seen that these predictions agree very well with the experimentally measured values of G_{Ic} at RT, but noticeably underestimate the fracture energy of the epoxy nanocomposites at -196°C. This underprediction can be attributed to the influence of thermal residual stresses, as discussed below in Section 4.4. Plastic void growth can be seen to be the most dominant toughening mechanism in Table 3, providing the majority of the improvement in the overall fracture energy of the epoxy nanocomposites. Consequently, accounting for the effect of compressive thermal residual stresses on the energy dissipation during the plastic void growth is of paramount importance in modelling the value of G_{Ic} at cryogenic temperatures.

In comparison to plastic void growth, the toughness enhancement due to nanorod pull-out only makes a minor contribution in the present work, as indicated in Table 3. This contrasts with previous work employing other 1D nanofillers i.e. CNFs [43, 44] and CNTs [48], in which pull-out was found to dissipate a comparable amount of energy to that of plastic void growth at RT. This difference can be explained by the CuO nanorods having a much lower aspect ratio (i.e. of ~6) compared with that of CNFs (i.e. of ~134 [44]) and CNTs (i.e. of ~1000 [48]) and from [51] there is a linear dependence of ΔG_{po} on the square of the pull-out length divided by the diameter of the nanofiller. Consequently, although the pull-out process may dissipate more energy at -196°C than at RT, due to the contribution of compressive residual stresses as well as the higher interfacial shear strength, τ_i, at cryogenic temperatures [47], the toughness contribution from this mechanism is still quite low due to the very limited pull-out length of the CuO nanorods. Furthermore, due to the relatively low volume fraction of nanorods that were used, the contributions from the shear yielding and debonding mechanisms to the overall fracture energy are also relatively modest. However, it should be noted that nanorod debonding plays a crucial role in initiating and promoting the plastic void growth of the epoxy matrix, as reported in previous work [14, 43].

4.4 Modification to fracture energy model

It is reasonable to expect that a compressive residual stress at the interface would increase the applied stress required to initiate debonding. Accordingly, a straightforward modification of the Williams et al. model [52] is to replace σ_c in Eqs. (4) and (7) by the term $\sigma_c + \sigma_r^T$ to account for the compressive thermal residual stress at -196°C, which leads to:

$$\Delta U_{db} = (1+v)\frac{(\sigma_c+\sigma_r^T)^2}{E_m}V_r \quad (8)$$

$$\Delta U_v = (1+v)\left[(V_{void}-V_{po})(\sigma_c+\sigma_r^T) - \frac{1}{(1-v)}\frac{(\sigma_c+\sigma_r^T)^2}{E_m}V_{po}\right] \quad (9)$$

where the thermal residual compressive radial stress again is given by σ_r^T and the modified height, h, of the dissipation zone is given by:

$$h = \frac{E_m G_{CU}}{2\pi(\sigma_c+\sigma_r^T)^2} \quad (10)$$

The predicted values of G_{Ic} at -196°C obtained by using these modifications for ΔU_{db} and ΔU_v, with the value of σ_r^T determined from the FEM analysis (see the Supplementary Information), and leaving the estimates for the other toughening mechanisms as previously given, are shown by the solid line in Fig 10b and in Table 3. It can be seen that including the effects of the thermal residual stresses now lead to a very good agreement between the predicted and the experimentally measured values of G_{Ic} at -196°C, as was the case for the tensile strength results at -196°C discussed in Section 4.1. Although a smaller dissipation zone is calculated from Eq. (10) at -196°C, than that at RT, it can be readily deduced from Eqs. (8), (9) that at cryogenic temperatures the presence of compressive radial thermal stresses due to CTE mismatch would increase the dissipated strain energy-densities provided the voids plastically grow to a certain size. Consequently, plastic void growth accounts for a comparable increase in G_{Ic} at -196°C as at RT (see Fig. 6d), and the enhanced values of ΔU_{db} and ΔU_v due to the presence of compressive residual stresses at -196°C are sufficient to compensate for any reduction in the size of the dissipation zone. This is an encouraging finding, as it may facilitate the selection of nano-reinforcements with the appropriate CTE for the design and optimisation of epoxy nanocomposites to reach the desired mechanical properties for cryogenic applications. In particular the negative, or ultra-low, CTE nano-reinforcements may be of major importance in toughening and strengthening the polymer matrix for FRPs at cryogenic temperatures, thus enabling their use in lightweight cryogenic storage vessels.

5. Conclusions

A method of strengthening and toughening an epoxy polymer at both RT and cryogenic temperatures by using CuO nanorods to produce epoxy nanocomposites has been presented. The nanorods were synthesized through a hydrothermal reaction process and found to exhibit a vanishing, or even a negative, CTE at cryogenic temperatures. The mechanical properties of the epoxy nanocomposites incorporating up to 8 wt% of CuO nanorods were investigated. Both the tensile strength and fracture energy

of the nanocomposites were observed to be significantly improved at both RT and at -196°C. Compared to the neat epoxy, the highest property enhancements were found for the epoxy nanocomposites containing 4 wt% of CuO nanorods, with the relative percentage improvements at RT and -196°C being 18% and 21%, respectively, for the ultimate tensile strength, and 132% and 262%, respectively, for the fracture energy. It is noteworthy that the dual improvements of strength and toughness are superior to those previously reported for other hard fillers at both RT and, especially, at cryogenic temperatures. Current theoretical models for the strength and the fracture energy were found to agree very well with the experimental results at RT, but significantly underpredicted the experimentally measured properties at -196°C. Modifications of these theoretical models were proposed to take into account the compressive thermal residual stress developed at the cryogenic temperature due to the CTE mismatch. These modified models were shown to then result in good agreement between the predictions and the measured values of the strength and toughness of the epoxy nanocomposites at -196°C. These novel nanorod/epoxy nanocomposites, as well as the modified formulae for predicting the cryogenic strength and toughness, will be useful in designing and optimising multi-scale fibre composites intended for cryogenic applications such as cryogenic fuel tanks.

Declaration of competing interest

The authors declare that they have no known competing financial interests or personal relationships that could have appeared to influence the work reported in this paper.

Acknowledgements

The authors are thankful for the financial support received from the Australian Research Council's Discovery Grant Program (DP190102790). The authors acknowledge the facilities and the scientific and technical assistance of Microscopy Australia at the Electron Microscope Unit (EMU) and X-ray Diffraction Laboratory within the Mark Wainwright Analytical Centre (MWAC) at UNSW Sydney.

References

[1] Z.-K. Chen, J.-P. Yang, Q.-Q. Ni, S.-Y. Fu, Y.-G. Huang, Reinforcement of epoxy resins with multi-walled carbon nanotubes for enhancing cryogenic mechanical properties, Polymer 50 (2009) 4753-4759.

[2] S. Kalia, S.-Y. Fu, Polymers at cryogenic temperatures, Springer, Berlin, Germany, 2013.

[3] R.O. Ritchie, The conflicts between strength and toughness, Nat. Mater. 10 (2011) 817-822.

[4] J. Meng, Y. Wang, H. Yang, P. Wang, Q. Lei, H. Shi, H. Lei, D. Fang, Mechanical properties and internal microdefects evolution of carbon fiber reinforced polymer composites: Cryogenic temperature and thermocycling effects, Compos. Sci. Technol. 191 (2020) 108083.

[5] Y. He, Q. Chen, S. Yang, C. Lu, M. Feng, Y. Jiang, G. Cao, J. Zhang, C. Liu, Micro-crack behavior of carbon fiber reinforced Fe_3O_4/graphene oxide modified epoxy composites for cryogenic application, Composites Part A 108 (2018) 12-22.

[6] R.E. Bilstein, Stages to Saturn: A technological history of the Apollo/Saturn launch vehicles, NASA History Office, United States, 1996.
[7] J.-P. Yang, G. Yang, G. Xu, S.-Y. Fu, Cryogenic mechanical behaviors of MMT/epoxy nanocomposites, Compos. Sci. Technol. 67 (2007) 2934-2940.
[8] C.J. Huang, S.Y. Fu, Y.H. Zhang, B. Lauke, L.F. Li, L. Ye, Cryogenic properties of SiO_2/epoxy nanocomposites, Cryogenics 45 (2005) 450-454.
[9] X.-J. Shen, Y. Liu, H.-M. Xiao, Q.-P. Feng, Z.-Z. Yu, S.-Y. Fu, The reinforcing effect of graphene nanosheets on the cryogenic mechanical properties of epoxy resins, Compos. Sci. Technol. 72 (2012) 1581-1587.
[10] C.-B. Qu, Y. Huang, F. Li, H.-M. Xiao, Y. Liu, Q.-P. Feng, G.-W. Huang, N. Li, S.-Y. Fu, Enhanced cryogenic mechanical properties of carbon fiber reinforced epoxy composites by introducing graphene oxide, Compos. Commun. 22 (2020) 100480.
[11] J.L. Li, C. Peng, Z.W. Li, Z.J. Wu, S.C. Li, The improvement in cryogenic mechanical properties of nano-ZrO_2/epoxy composites via surface modification of nano-ZrO_2, RSC Adv. 6 (2016) 61393-61401.
[12] S. Li, D. Chen, C. Gao, Y. Yuan, H. Wang, X. Liu, B. Hu, J. Ma, M. Liu, Z. Wu, Epoxy-functionalized polysiloxane/Nano-SiO_2 synergistic reinforcement in cryogenic mechanical properties of epoxy and carbon fiber reinforced epoxy laminate, Compos. Sci. Technol. 198 (2020) 108292.
[13] L. Jia, P. Qi, K. Shi, X. Liu, W. Ma, S. Lin, F. Zhang, X. Jia, Q. Cai, X. Yang, High performance epoxy-based composites for cryogenic use: A approach based on synergetic strengthening effects of epoxy grafted polyurethane and MWCNTs-NH_2, Compos. Sci. Technol. 184 (2019) 107865.
[14] T.H. Hsieh, A.J. Kinloch, K. Masania, A.C. Taylor, S. Sprenger, The mechanisms and mechanics of the toughening of epoxy polymers modified with silica nanoparticles, Polymer 51 (2010) 6284-6294.
[15] D. Carolan, A. Ivankovic, A.J. Kinloch, S. Sprenger, A.C. Taylor, Toughened carbon fibre-reinforced polymer composites with nanoparticle-modified epoxy matrices, J. Mater. Sci. 52 (2016) 1767-1788.
[16] N.R. Council, Accelerated aging of materials and structures: The effects of long-term elevated-temperature exposure, National Academies Press, Washington, DC, 1996.
[17] M.M. Shokrieh, A. Daneshvar, S. Akbari, Reduction of thermal residual stresses of laminated polymer composites by addition of carbon nanotubes, Mater. Des. 53 (2014) 209-216.
[18] X.G. Zheng, H. Kubozono, H. Yamada, K. Kato, Y. Ishiwata, C.N. Xu, Giant negative thermal expansion in magnetic nanocrystals, Nat. Nanotechnol. 3 (2008) 724-726.
[19] H. Yamada, X.-G. Zheng, Y. Soejima, M. Kawaminami, Lattice distortion and magnetolattice coupling in CuO, Phys. Rev. B 69 (2004) 104104.
[20] T. Koshi, Negative thermal expansion materials: technological key for control of thermal expansion, Sci. Technol. Adv. 13 (2012) 013001.
[21] Q. Zhang, K. Zhang, D. Xu, G. Yang, H. Huang, F. Nie, C. Liu, S. Yang, CuO nanostructures: Synthesis, characterization, growth mechanisms, fundamental properties, and applications, Prog. Mater Sci. 60 (2014) 208-337.
[22] B. Polyakov, L.M. Dorogin, S. Vlassov, M. Antsov, P. Kulis, I. Kink, R. Lohmus, In situ measurements of ultimate bending strength of CuO and ZnO nanowires, Eur. Phys. J. B 85 (2012) 366.
[23] E.P.S. Tan, Y. Zhu, T. Yu, L. Dai, C.H. Sow, V.B.C. Tan, C.T. Lim, Crystallinity and surface effects on Young's modulus of CuO nanowires, Appl. Phys. Lett. 90 (2007) 163112.
[24] Y. Huang, A.J. Kinloch, Modelling of the toughening mechanisms in rubber-modified epoxy polymers Part I, J. Mater. Sci. 27 (1992) 2753-2762.
[25] Y. Huang, A.J. Kinloch, Modelling of the toughening mechanisms in rubber-modified epoxy polymers Part II, J. Mater. Sci. 27 (1992) 2763-2769.
[26] K.M. Shrestha, C.M. Sorensen, K.J. Klabunde, Synthesis of CuO nanorods, reduction of CuO into Cu nanorods, and diffuse reflectance measurements of CuO and Cu nanomaterials in the near infrared region, J. Phys. Chem. C 114 (2010) 14368-14376.

[27] RAMPF, RAKUTOOL EL-2203/EH-2970 Epoxy Laminating System, 2017. https://www.rampf-group.com/fileadmin/rampf-gruppe.de/media/tooling_solutions/tds_GB/EL-2203-EH-2970-1-GB-epoxy-infusion-system-product-datasheet.pdf. (Accessed 19 September 2020).
[28] I.B. Krynetskiĭ, B.A. Gizhevskiĭ, S.V. Naumov, E.A. Kozlov, Size effect of the thermal expansion of nanostructural copper oxide, Phys. Solid State 50 (2008) 756-758.
[29] ASTM D638–14, Standard test method for tensile properties of plastics, ASTM International, West Conshohocken, United States, 2014.
[30] ISO 25217, Adhesives - determination of the mode I adhesive fracture energy of structural adhesive joints using double cantilever beam and tapered double cantilever beam specimens, Geneva, Switzerland, 2009.
[31] M. Vert, Y. Doi, K.-H. Hellwich, M. Hess, P. Hodge, P. Kubisa, M. Rinaudo, F. Schué, Terminology for biorelated polymers and applications (IUPAC Recommendations 2012), Pure Appl. Chem. 84 (2012) 377-410.
[32] Q. Feng, J. Yang, Y. Liu, H. Xiao, S. Fu, Simultaneously enhanced cryogenic tensile strength, ductility and impact resistance of epoxy resins by polyethylene glycol, J. Mater. Sci. Technol. 30 (2014) 90-96.
[33] A.R. Ravindran, R.B. Ladani, A. Zavabeti, T. Daeneke, S. Wu, A.J. Kinloch, C.H. Wang, K. Kalantar-Zadeh, A.P. Mouritz, Liquid metal synthesis of two-dimensional aluminium oxide platelets to reinforce epoxy composites, Compos. Sci. Technol. 181 (2019) 107708.
[34] E.C. Botelho, M.L. Costa, E.R. Edwards, T. Burkhart, B. Lauke, Effects of carbon nanotube fillers dispersion on mechanical behavior of phenolic/carbon nanotube nanocomposite, J. Mater. Res. 27 (2012) 2342-2351.
[35] S. Wu, S. Peng, C.H. Wang, Multifunctional polymer nanocomposites reinforced by aligned carbon nanomaterials, Polymers 10 (2018) 542.
[36] K. Jayaraman, M. Kortschot, Correction to the Fukuda-Kawata Young's modulus theory and the Fukuda-Chou strength theory for short fibre-reinforced composite materials, J. Mater. Sci. 31 (1996) 2059-2064.
[37] S. Mortazavian, A. Fatemi, Effects of fiber orientation and anisotropy on tensile strength and elastic modulus of short fiber reinforced polymer composites, Composites Part B 72 (2015) 116-129.
[38] A. Kelly, W.R. Tyson, Tensile properties of fibre-reinforced metals: copper/tungsten and copper/molybdenum, Journal of the Mechanics Physics of Solids 13 (1965) 329-350.
[39] M.R. Piggott, Short fibre polymer composites: a fracture-based theory of fibre reinforcement, J. Compos. Mater. 28 (1994) 588-606.
[40] L.-C. Tang, Y.-J. Wan, D. Yan, Y.-B. Pei, L. Zhao, Y.-B. Li, L.-B. Wu, J.-X. Jiang, G.-Q. Lai, The effect of graphene dispersion on the mechanical properties of graphene/epoxy composites, Carbon 60 (2013) 16-27.
[41] A. Guevara-Morales, A. Taylor, Mechanical and dielectric properties of epoxy–clay nanocomposites, J. Mater. Sci. 49 (2014) 1574-1584.
[42] H. Zhang, L. Tang, G. Liu, D. Zhang, L. Zhou, Z. Zhang, The effects of alumina nanofillers on mechanical properties of high-performance epoxy resin, J. Nanosci. Nanotechnol. 10 (2010) 7526-7532.
[43] R.B. Ladani, S. Wu, A.J. Kinloch, K. Ghorbani, J. Zhang, A.P. Mouritz, C.H. Wang, Improving the toughness and electrical conductivity of epoxy nanocomposites by using aligned carbon nanofibres, Compos. Sci. Technol. 117 (2015) 146-158.
[44] A.R. Ravindran, R.B. Ladani, S. Wu, A.J. Kinloch, C.H. Wang, A.P. Mouritz, Multi-scale toughening of epoxy composites via electric field alignment of carbon nanofibres and short carbon fibres, Compos. Sci. Technol. 167 (2018) 115-125.
[45] S.-Y. Fu, X. Hu, C.-Y. Yue, Effects of fiber length and orientation distributions on the mechanical properties of short-fiber-reinforced polymers, Mater. Sci. Res. Int. 5 (1999) 74-83.
[46] S.-Y. Fu, B. Lauke, Effects of fiber length and fiber orientation distributions on the tensile strength of short-fiber-reinforced polymers, Compos. Sci. Technol. 56 (1996) 1179-1190.
[47] Y. Jia, W. Yan, H.-Y. Liu, Carbon fibre pullout under the influence of residual thermal stresses in polymer matrix composites, Comput. Mater. Sci. 62 (2012) 79-86.

[48] T.H. Hsieh, A.J. Kinloch, A.C. Taylor, I.A. Kinloch, The effect of carbon nanotubes on the fracture toughness and fatigue performance of a thermosetting epoxy polymer, J. Mater. Sci. 46 (2011) 7525-7535.
[49] T.H. Hsieh, A.J. Kinloch, K. Masania, J. Sohn Lee, A.C. Taylor, S. Sprenger, The toughness of epoxy polymers and fibre composites modified with rubber microparticles and silica nanoparticles, J. Mater. Sci. 45 (2009) 1193-1210.
[50] T. Clyne, D. Hull, An introduction to composite materials, Third Ed., Cambridge University Press, Cambridge, United Kingdom, 2019.
[51] J.-K. Kim, Y.-W.J.C.S. Mai, Technology, High strength, high fracture toughness fibre composites with interface control—a review, 41 (1991) 333-378.
[52] J.G. Williams, B.R.K. Blackman, H. Steininger, K. Zuo, Toughening by plastic cavitation around cylindrical particles and fibres, Compos. Sci. Technol. 103 (2014) 119-126.
[53] J.G. Williams, Particle toughening of polymers by plastic void growth, Compos. Sci. Technol. 70 (2010) 885-891.
[54] B. Lauke, On the effect of particle size on fracture toughness of polymer composites, Compos. Sci. Technol. 68 (2008) 3365-3372.
[55] S. He, D. Carolan, A. Fergusson, A.C. Taylor, Toughening epoxy syntactic foams with milled carbon fibres: Mechanical properties and toughening mechanisms, Mater. Des. 169 (2019) 107654.

Figures and Tables

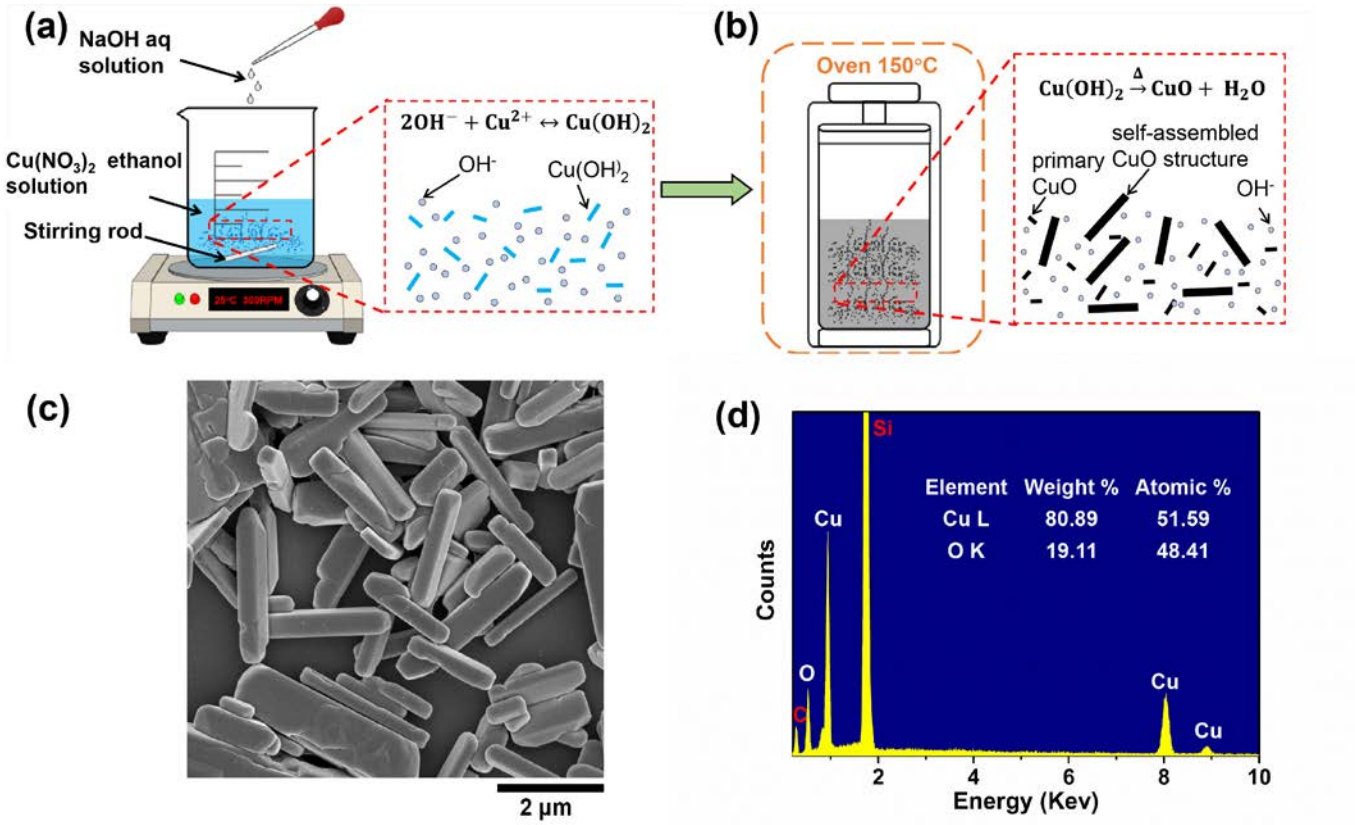


Fig. 1 Schematic depicting the hydrothermal synthesis process of the CuO nanorods: (a) addition of NaOH aqueous solution to the $Cu(NO_3)_2$ ethanol solution; (b) transfer the reaction solution to a Teflon-lined autoclave and keep at 150°C for 24 h; (c) SEM micrograph of the CuO nanorods and (d) EDX elemental analysis of the synthesized CuO nanorods.

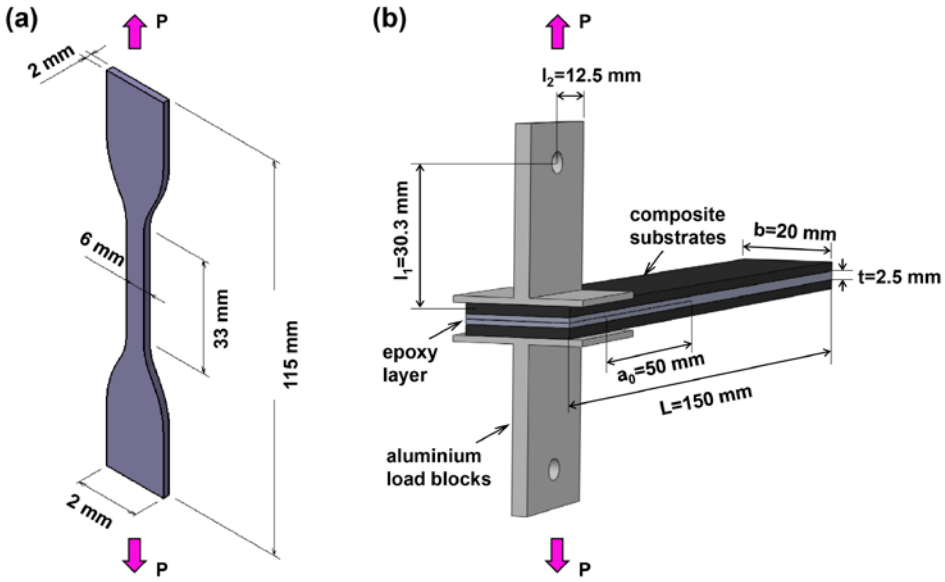


Fig. 2 Schematic of (a) the tensile test specimen and (b) the DCB-bonded joint specimen.

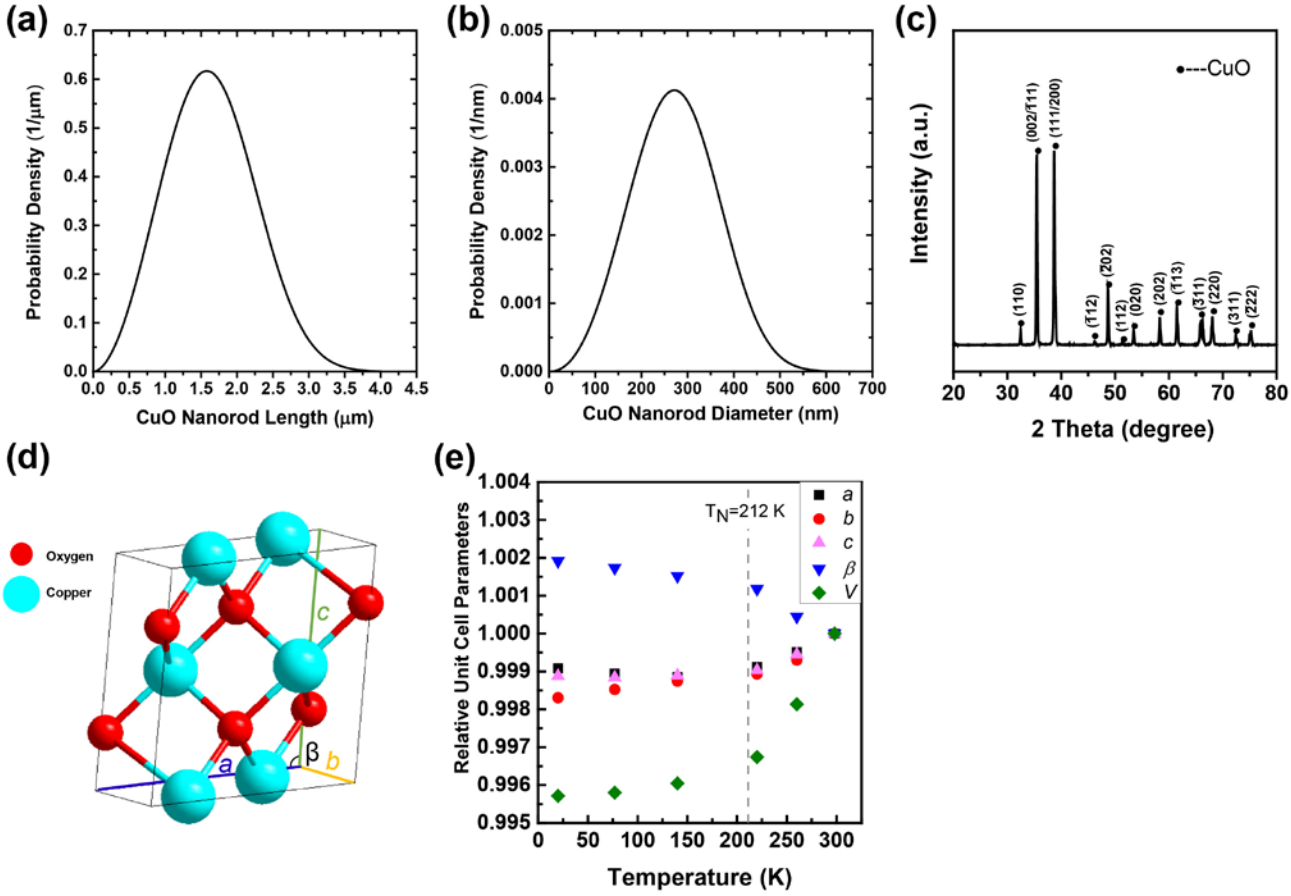
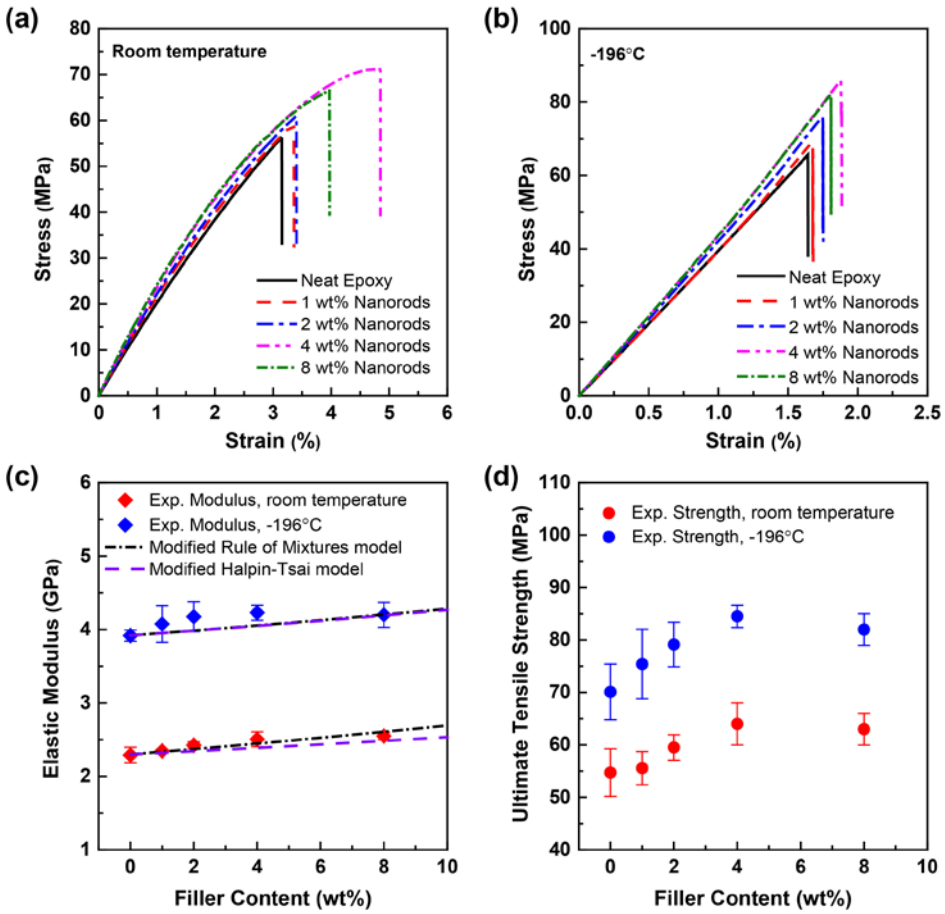
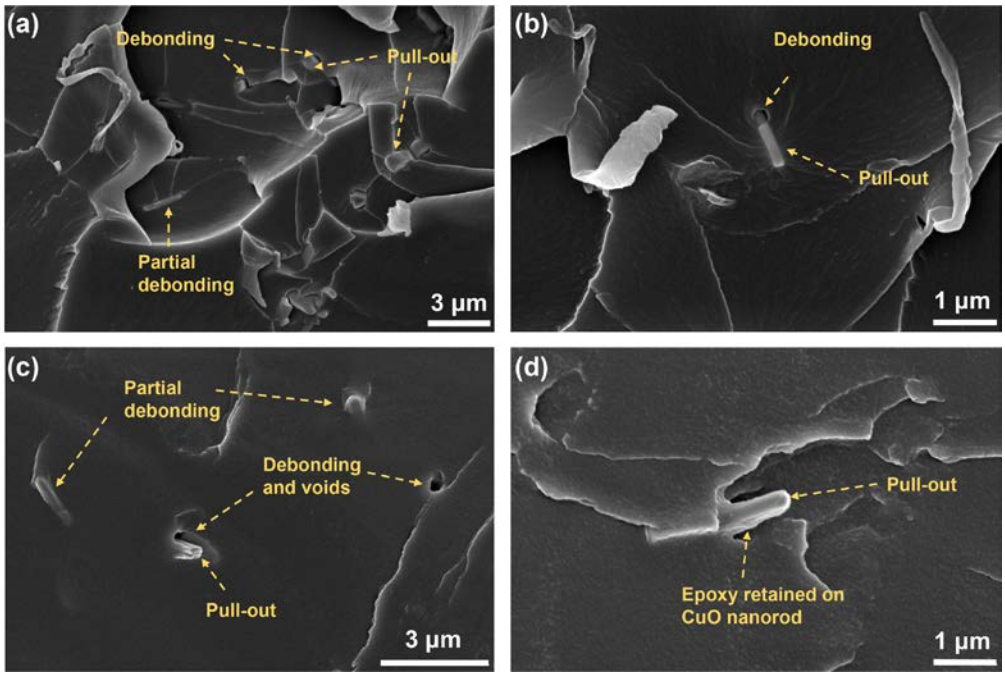


Fig. 3 (a) Length probability density function of CuO nanorods measured from SEM micrographs i.e. Fig. 1c and Fig. S2; (b) diameter probability density function of CuO nanorods measured from SEM micrographs i.e. Fig. 1c and Fig. S2; (c) XRD pattern of CuO nanorods measured at ambient temperature; (d) schematic of CuO unit cell illustrating monoclinic crystal structure; (e) temperature dependence of the lattice parameters for CuO nanorods relative to the values obtained at RT and *V* is the unit cell volume.



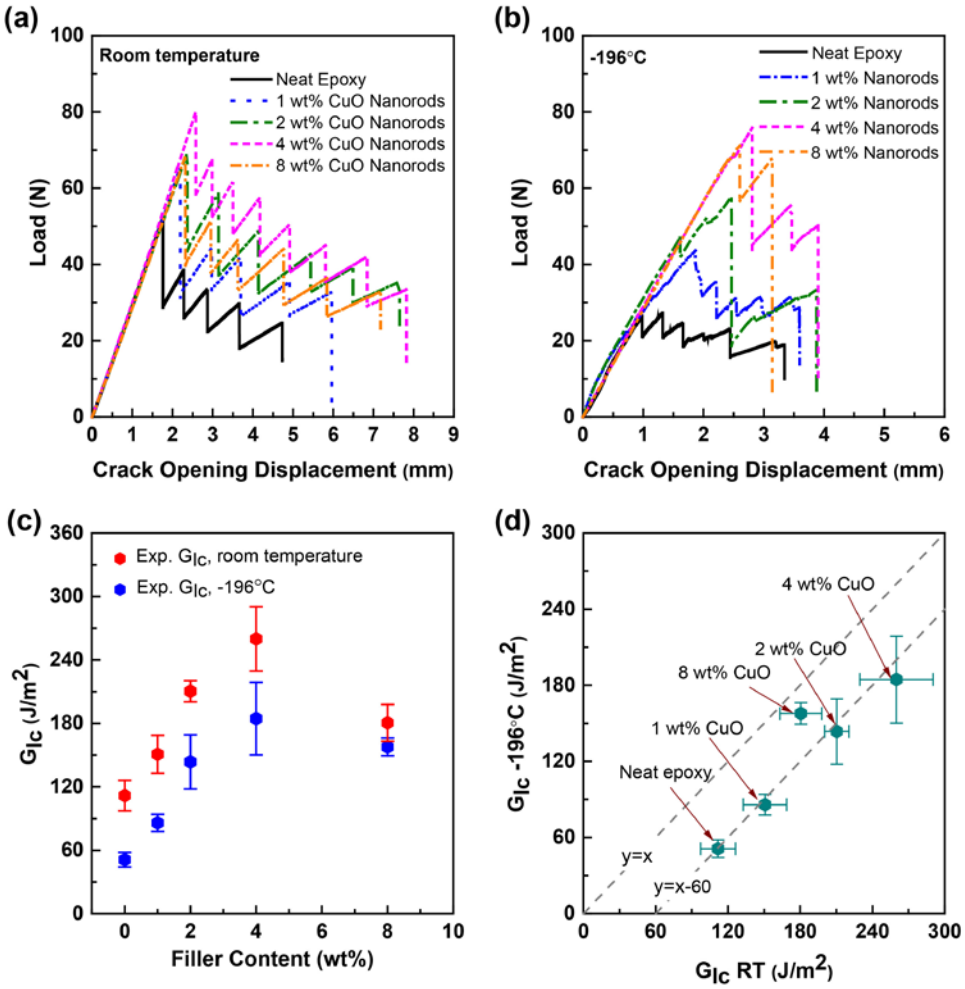
602

603 **Fig. 4** Tensile stress versus strain curves obtained at (a) RT and (b) -196°C for the epoxy with different
604 weight contents of CuO nanorods. The effect of increasing the weight content of CuO nanorods (c) on the
605 Young's modulus and comparison with model predictions, and (d) on the ultimate tensile strength.



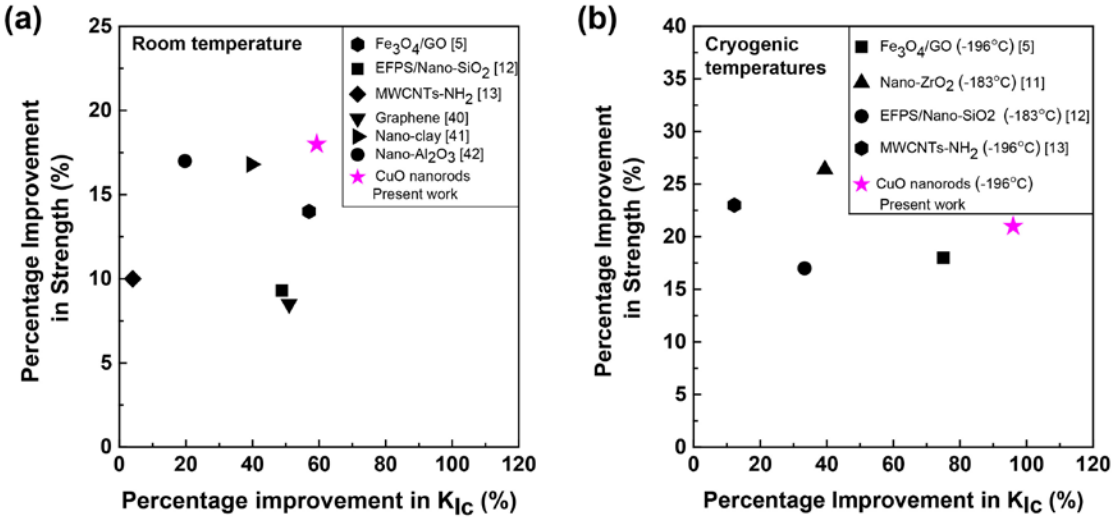
606

607 **Fig. 5** SEM micrographs of the fracture surfaces from the tensile tests of the epoxy nanocomposites
608 containing 4wt% CuO nanorods tested at (a)-(b) RT and (c)-(d) -196°C.



609

610 **Fig. 6** Load versus displacement curves for neat epoxy and epoxy nanocomposites containing different
611 weight fractions of CuO nanorods measured at (a) RT and (b) -196°C; (c) effect of CuO nanorod content
612 on the measured G_{Ic} of the epoxy polymers at RT and -196°C; (d) comparison of the measured G_{Ic} of the
613 epoxy polymers at RT and -196°C. (Note: the dashed lines have a slope of 1 to aid data interpretation.)



614

615 **Fig. 7** Relative percentage improvements in strength plotted against the mode I fracture toughness, K_{Ic}, of
616 the nanocomposites studied in the present work and other reported epoxy composites containing hard
617 nano/micro fillers at (a) RT and (b) cryogenic temperatures. (Note: Only the highest property enhancements
618 in each study are considered and the K_{Ic} values from the present study were calculated using, $K_{Ic} =$
619 $\sqrt{G_{Ic} \times E_{com}/(1-\nu^2)}$.)

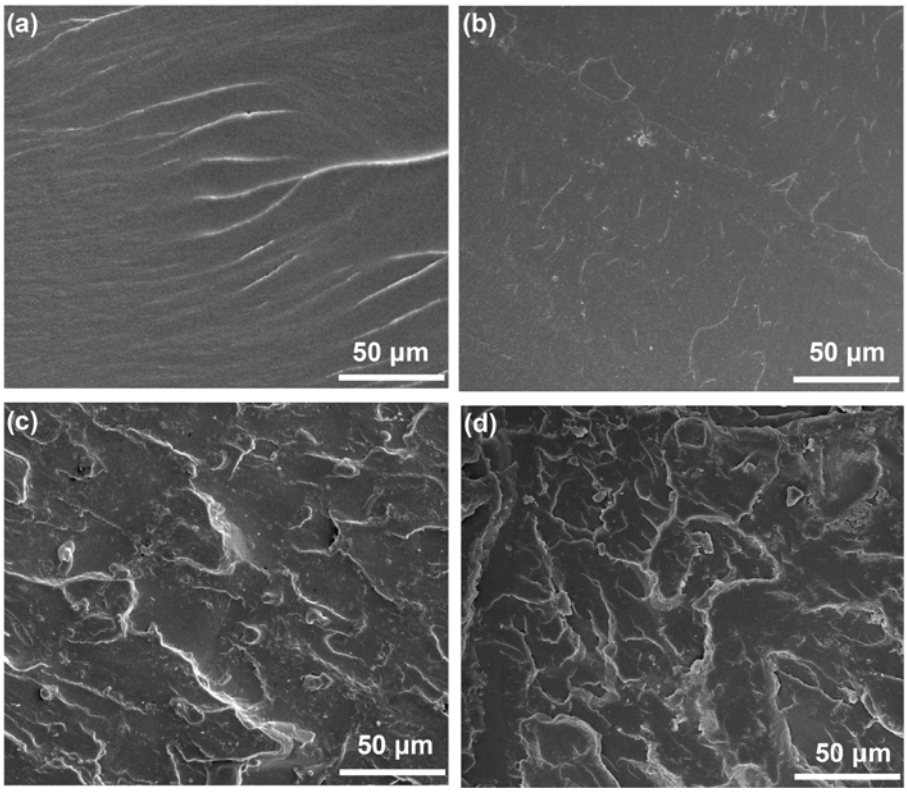


Fig. 8 SEM micrographs of the crack initiation region of the fracture surfaces at low magnification for the neat epoxy at (a) RT and (b) -196°C; and for the epoxy nanocomposites containing 4wt% CuO nanorods at (c) RT, (d) -196°C. (Note: In all cases, the crack-front propagation direction is from left to right.)

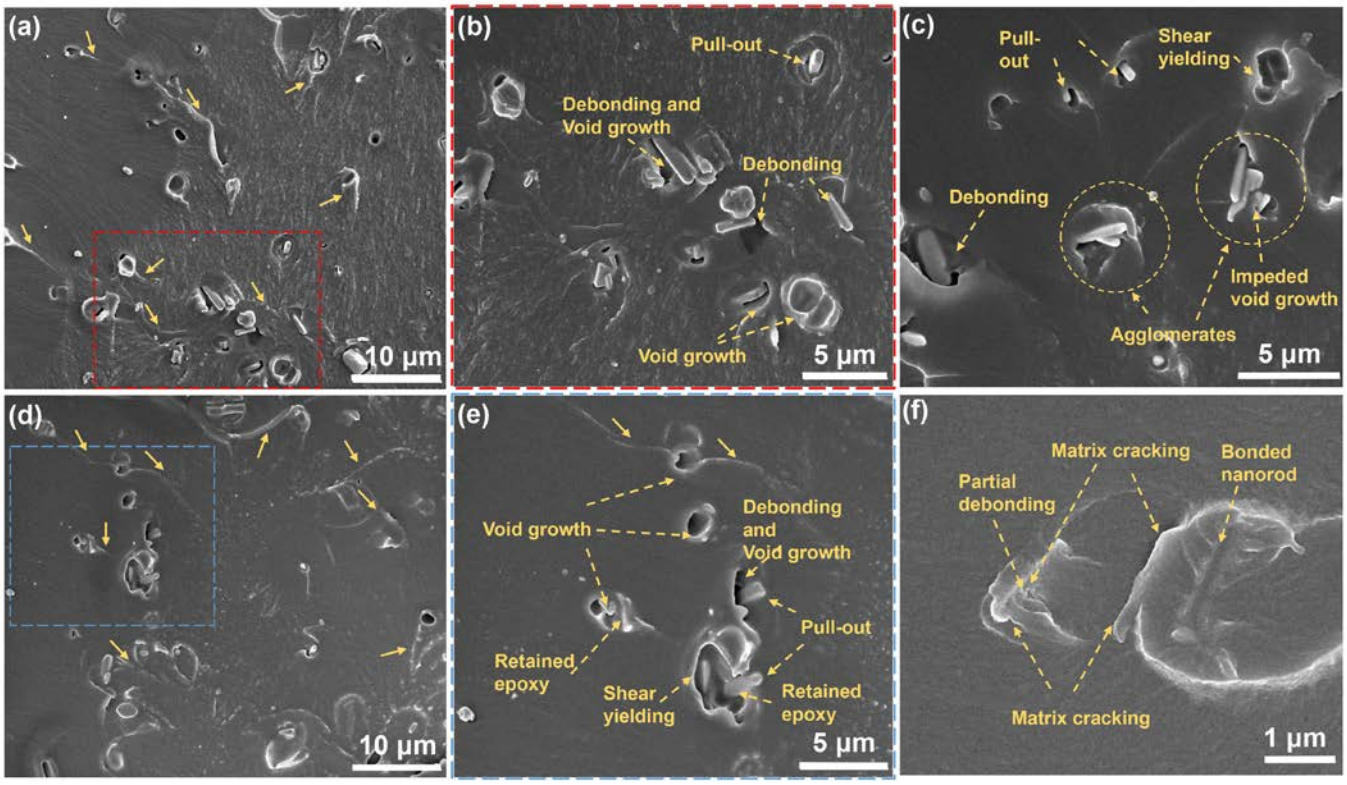
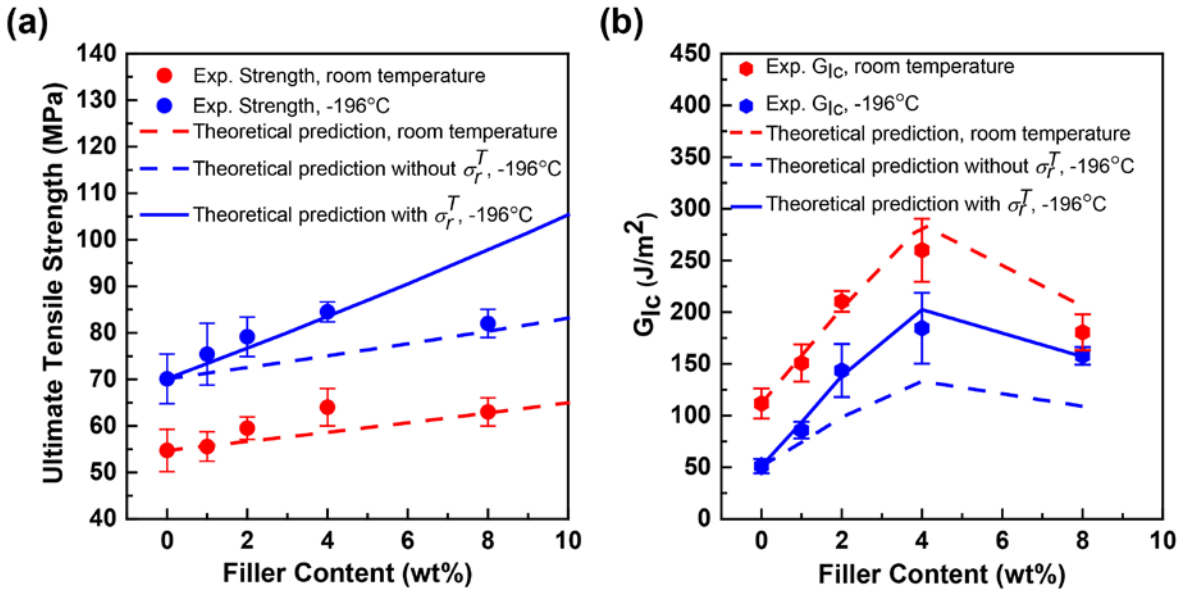


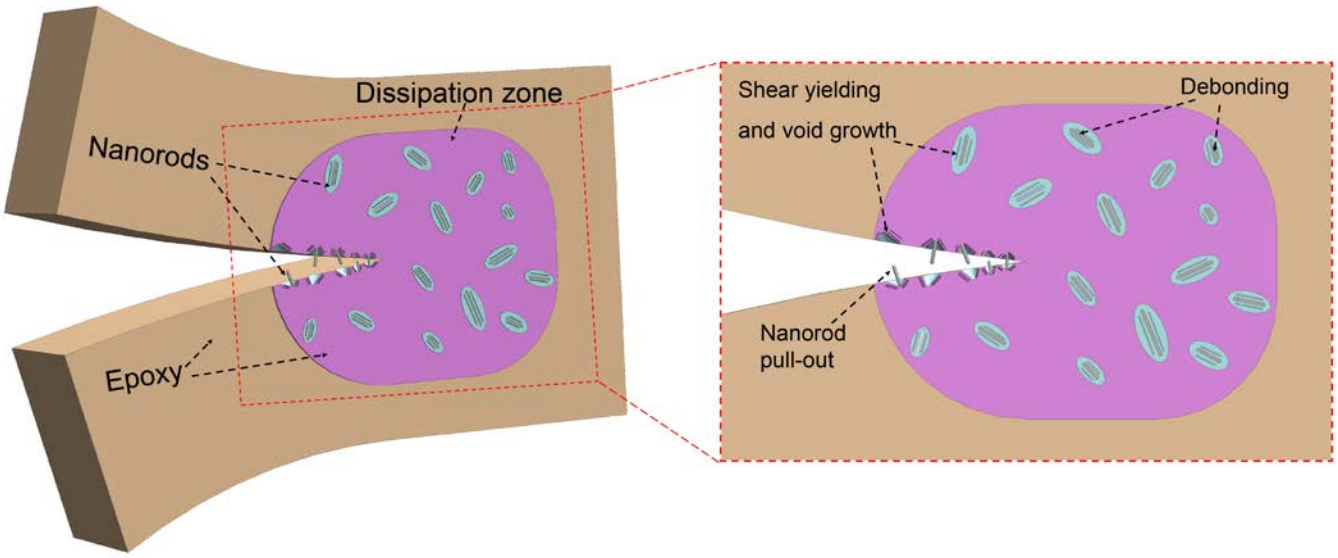
Fig. 9 SEM micrographs of the crack initiation region of the fracture surfaces at high magnifications for (a) epoxy nanocomposites containing 4 wt% CuO nanorods fractured at RT; (b) is the magnified image taken from the red rectangular region; (c) epoxy nanocomposites containing 8 wt% CuO nanorods fractured at RT; (d) epoxy nanocomposites containing 4 wt% CuO nanorods fractured at -196°C; (e) is the magnified image taken from the blue rectangular region; (f) region of epoxy nanocomposites containing nanorods oriented parallel with the fracture surface at -196°C. (Note: In all cases, the crack-front propagation direction is from left to right. The short solid yellow arrows indicate the tail structures.)



633

634 **Fig. 10** Comparison between the theoretical predictions and experimental results for (a) the tensile strength

635 and (b) the fracture energy at RT and -196°C.



636

637 **Fig. 11** Schematic illustrations of the toughening mechanisms exhibited by the epoxy nanocomposites

638 containing CuO nanorods.

639

Table 1

CTE values of synthesized CuO nanorod

Direction	Symbol	CTE, 20 to 212 K (10^{-6} K^{-1})	CTE, 212 to 298 K (10^{-6} K^{-1})	Mean CTE, 77 to 298 K (10^{-6} K^{-1})
Axial	α_1	4.46	9.18	5.70
Transverse	α_2	-1.31	7.05	3.80
Transverse	α_3	1.93	13.1	6.75

640

Table 2

List of values for the parameters used in the fracture energy modelling studies

Parameter	Symbol	Unit	Value for RT estimate	Value for -196°C estimate	Source
Nanorod average diameter	d_r	nm	272	272	Present study
Nanorod average length	l_{mean}	μm	1.65	1.65	Present study
Effective pull-out length	l_{po}	μm	0.83	0.83	Present study
Density of the CuO	ρ_r	g/cm^3	6.31	6.31*	[21]
Density of neat epoxy	ρ_m	g/cm^3	1.11	1.11*	[27]
Critical stress initiating debonding and void	σ_c	MPa	54.7	70.1	Present study
Thermal residual compressive radial stress	σ_r^T	MPa	0	60	Present study
Poisson's ratio of epoxy	ν	-	0.35	0.35*	[14]
Young's modulus of neat epoxy	E_m	GPa	2.3	3.9	Present study
Pressure dependent yield stress constant	μ_m	-	0.2	0.2*	[43]
Fracture energy of neat epoxy	G_{CU}	J/m^2	111.7	51.1	Present study
True failure strain of neat epoxy	γ	%	3.2	1.7	Present study

*Assumed to be equal to the value for RT analysis

641

642

Table 3

Predicted G_{Ic} values compared to the measured* values at RT and -196°C

Test temperature	Nanorods (wt%)	V_r (%)	V_{po} (%)	ΔG_v (J/m^2)	ΔG_s (J/m^2)	ΔG_{db} (J/m^2)	ΔG_{po} (J/m^2)	Predicted G_{Ic} (J/m^2)	Measured* G_{Ic} (J/m^2)
RT	1	0.18	0.13	45.2	0.7	0.1	0.2	157.9	150.8
	2	0.36	0.25	90.5	1.0	0.2	0.4	203.7	210.4
	4	0.73	0.47	170.4	1.5	0.4	0.7	284.6	259.9
	8	1.51	0.76	90.0	2.3	0.7	1.1	205.8	180.5
-196°C without σ_r^T	1	0.18	0.12	22.5	0.2	0.1	0.2	74.1	85.9
	2	0.36	0.25	46.4	0.3	0.1	0.5	98.4	143.6
	4	0.73	0.44	80.7	0.5	0.2	0.8	133.2	184.5
	8	1.51	0.75	55.5	0.8	0.3	1.3	109.0	157.8
-196°C with σ_r^T	1	0.18	0.12	41.8	0.2	0.1	0.2	93.5	85.9
	2	0.36	0.25	86.1	0.3	0.3	0.5	138.2	143.6
	4	0.73	0.44	149.6	0.5	0.6	0.8	202.5	184.5
	8	1.51	0.75	102.6	0.8	1.1	1.3	157.0	157.8

643 *Note: only the mean values of the measured values of G_{Ic} are provided here. The measured mean values
644 and the associated standard deviations are given, and discussed, in the Supplementary Information.
645